The Astrophysical Journal, 992:180 (8pp), 2025 October 20 https://doi.org/10.3847/1538-4357/ae08b4


# Estimation of Effective Viscosity to Quantify Collisional Behavior in Collisionless Plasma

Subash Adhikari[1], Carlos A. González[2], Yan Yang (杨艳)[1], Sean Oughton[3], Francesco Pecora[1], Riddhi Bandyopadhyay[1,4], and William H. Matthaeus[1]
[1] Department of Physics and Astronomy, University of Delaware, Newark, DE 19716, USA; subash@udel.edu
[2] Department of Physics, The University of Texas at Austin, Austin, TX 78712, USA
[3] Department of Mathematics, University of Waikato, Hamilton 3240, New Zealand
[4] Department of Astrophysical Sciences, Princeton, NJ 08544, USA
*Received 2025 August 11; revised 2025 September 16; accepted 2025 September 16; published 2025 October 14*

## Abstract

While dissipation in collisional plasma is defined in terms of viscosity and resistivity, the exact functional form of dissipation, i.e., the so-called dissipation function in nearly collisionless plasma, is unknown. Nevertheless, previous studies have suggested that there exists viscous-like energy conversion in collisionless plasma with scaling characteristics analogous to collisional plasma, and in particular that the average dissipation is proportional to the square of the rate of strain as in hydrodynamics. In this study, using 2.5D kinetic particle-in-cell (PIC) simulation of collisionless plasma turbulence, we provide an estimate of effective viscosity at each scale, obtained via a scale-filtering approach. We then compare the turbulent dynamics of the PIC simulation with that from MHD and two-fluid simulations in which the viscosity is equal to the effective viscosity estimate obtained from the PIC simulation. We find that the global behavior in these MHD and two-fluid simulations has a striking similarity to that in their kinetic/PIC counterpart. In addition, we explore the scale dependence of the effective viscosity and discuss implications of this approach for space plasmas.

*Unified Astronomy Thesaurus concepts:* Space plasmas (1544); Collisional processes (2286)

## 1. Introduction

A fundamental assumption regarding dissipation in collisional plasmas is that Coulomb collisions are strong enough to drive the system to a local equilibrium. However, in many (nearly) collisionless plasmas this is not true, since such plasmas have very long collisional mean free paths and are therefore not able to "quickly" establish local equilibrium. As a result, the standard closures often employed in the collisional case, which relate energy dissipation to viscosity and resistivity, are inapplicable to nearly collisionless plasmas (S. Braginskii 1965).

Intriguingly, however, power spectra obtained from nearly collisionless plasma systems, such as the solar wind or appropriate numerical simulations, display behavior similar to that of hydrodynamic (i.e., strongly collisional) turbulence. For example, the wavenumber spectra often display an inertial range with a Kolmogorov-like $k^{-5/3}$ scaling, followed by a sharp transition to steeper spectra at larger wavenumbers, suggesting that the "collisionless" plasma may not be perfectly collisionless in a strict sense. In addition, recent advances connected with simulations and high-resolution spacecraft observations have suggested that pressure–strain interaction can describe the energy transfer at smaller kinetic scales and therefore represents the dissipation function in collisionless plasma processes, such as turbulence (Y. Yang et al. 2022) and reconnection (S. Adhikari et al. 2024). These features illustrate that (nearly) collisionless plasma can in fact behave in ways that are analogous to collisional dynamics, a subject that has a long history in kinetic theory estimations of anomalous resistivity (F. Coroniti 1980). Here we explore the possibility that one may quantify collisional-like effects, even potentially achieving a collisionless closure that captures dissipation in the case of collisionless turbulence (W. H. Matthaeus et al. 2020; O. Pezzi et al. 2021).

Traditionally it has not been uncommon to find the electromagnetic work $\boldsymbol{j}\cdot\boldsymbol{E}$ identified as a measure of dissipation—a practice particularly familiar in the reconnection community (S. Zenitani et al. 2011). However, examination of the Vlasov–Maxwell (VM) system (Y. Yang et al. 2017, 2019) reveals that while the rate of conversion of electromagnetic energy into kinetic energy is indeed determined by $\boldsymbol{j}\cdot\boldsymbol{E}$, the species-dependent pressure–strain interaction provides the channels for conversion of flow energy into the internal energy of the respective species. Both electromagnetic work and pressure–strain are integral to understanding the cascade and pathways to dissipation, and research has progressed on both. Several recent studies (R. Bandyopadhyay et al. 2023; Y. Yang et al. 2024b) have explicitly shown that the average of the electromagnetic work $\boldsymbol{j}\cdot\boldsymbol{E}$ (S. Zenitani et al. 2011) scales as the square of the electric current density, $\boldsymbol{j}^2$, when conditioned over $|\boldsymbol{j}|$. Similarly, the average of one of the ingredients of pressure–strain interaction (also called pressure work), when conditioned on a threshold of $D$, has been shown to scale as the (trace of the) squared velocity strain rate tensor, $D^2 = \mathsf{S}_{ij}\mathsf{S}_{ji}$ (see Section 2 for definitions). These results suggest the existence of collisional-*like* dissipation in so-called collisionless plasmas. Moreover, they enable quantification of effective viscosity and resistivity in collisionless plasma, which may then be used to help provide relevant estimates of energy dissipation. However, neither of these results involving conditional averages of the dissipation provide pointwise relationships between local dissipation and the respective dissipation coefficients. Likewise, the conditional averages provide no information about the scale dependence of the transport coefficients. Both of these

deficiencies are resolved for the viscous transport in the present alternative strategy. In this study, we consider a different approach to obtain estimates for effective ion viscosity—based on a scale-filtering technique—by examining the evolution of bulk flow energy using two different plasma models: magnetohydrodynamics (MHD) and VM. By comparing the different terms in their respective energy evolution equations, we obtain an analogy between them that leads to an estimate for an effective viscosity.

## 2. Theory

Before diving into the specifics of this study, we provide a brief overview of the scale-filtering technique. Scale filtering (M. Germano 1992) is based on a properly defined filtering kernel $G_\ell = \ell^{-d} G(\boldsymbol{r}/\ell)$, which, when convolved with any field $f(\boldsymbol{x}, t)$, only maintains information about $f$ at length scales larger than the filtering scale $\ell$. Here $G(\boldsymbol{r})$ is a normalized window function, usually chosen to be spatially compact, that satisfies $\int d^d r\, G(\boldsymbol{r}) = 1$, where $d$ is the number of dimensions of the system. For this study, we employ a nonnegative boxcar (aka top hat) function for $G$. The scale-filtered version of $f$, denoted $\overline{f}_\ell(\boldsymbol{x}, t)$ is defined as the convolution

$$\bar{f}_\ell(\boldsymbol{x}, t) = \int d^d r\, G_\ell(\boldsymbol{r}) f(\boldsymbol{x} + \boldsymbol{r}, t). \tag{1}$$

In situations where it is clear from context that the filterscale is $\ell$, we will often use $\overline{f}$ to mean $\overline{f}_\ell$.

Likewise, the density-weighted scale filtering of $f(\boldsymbol{x}, t)$ is defined as (note the tilde)

$$\widetilde{f}_\ell(\boldsymbol{x}, t) = \frac{\overline{[\rho(\boldsymbol{x}, t) f(\boldsymbol{x}, t)]}_\ell}{\overline{\rho}_\ell(\boldsymbol{x}, t)}, \tag{2}$$

where $\rho(\boldsymbol{x}, t)$ is the mass density. This is also called the Favre-filtered field (A. Favre 1969; H. Aluie 2013).

Using these techniques, one can obtain evolution equations for the scale-filtered kinetic energy associated with MHD and VM models. These equations, and in particular their terms related to dissipation, will form the basis of the analysis below.

### 2.1. Incompressible MHD Formalism

In incompressible MHD, the time evolution of the coarse-grained kinetic energy density (H. Aluie 2017) at any scale $\ell$ obeys

$$\partial_t E_f^{\mathrm{MHD}} + \nabla \cdot \boldsymbol{J}_u^{\mathrm{MHD}} = -\Pi_u^{\mathrm{MHD}} - \Lambda_{ub}^{\mathrm{MHD}} - 2\mu \overline{\mathsf{S}} \colon \overline{\mathsf{S}}. \tag{3}$$

Here, $E_f^{\mathrm{MHD}} = \rho \frac{|\bar{\boldsymbol{u}}|^2}{2}$ is the filtered kinetic energy density per unit volume associated with the coarse-grained bulk flow velocity $\bar{\boldsymbol{u}}$, where the mass density of the fluid is $\rho$. Likewise, $\boldsymbol{J}_u^{\mathrm{MHD}} = (\rho \frac{|\bar{\boldsymbol{u}}|^2}{2} + \overline{P})\bar{\boldsymbol{u}} + \overline{\tau} \cdot \bar{\boldsymbol{u}} - (\bar{\boldsymbol{u}} \cdot \bar{\boldsymbol{b}})\bar{\boldsymbol{b}} - \mu \nabla(\frac{|\bar{\boldsymbol{u}}|^2}{2})$ is related to various contributions to the transport of filtered kinetic energy. This includes the advective flux of large-scale kinetic energy, the influence of the Poynting flux, involving the coarse-grained magnetic field $\bar{\boldsymbol{b}}$, the filtered total scalar pressure $\overline{P}$, the subfilterscale nonlinear stresses $\overline{\tau}$, defined as the sum of the subscale Reynolds stress $\overline{\tau}^u = \rho[\overline{\boldsymbol{u}\boldsymbol{u}} - \bar{\boldsymbol{u}}\,\bar{\boldsymbol{u}}]$, and the subscale Maxwell stress $\overline{\tau}^b = -[\overline{\boldsymbol{b}\boldsymbol{b}} - \bar{\boldsymbol{b}}\,\bar{\boldsymbol{b}}]$. $\overline{\tau}$ characterizes the force acting on scales larger than $\ell$ due to fluctuations occurring at scales less than $\ell$, and $\mu$ is the dynamic viscosity. Similarly, the first term on the right-hand side (RHS), $\Pi_u^{\mathrm{MHD}} = -\overline{\mathsf{S}} \colon \overline{\tau}$, is the subgrid-scale kinetic energy flux that quantifies the transfer of kinetic energy across scales $\ell$, where $\mathsf{S}$ is the rate-of-strain tensor with $\overline{\mathsf{S}} = (\nabla \bar{\boldsymbol{u}} + \nabla \bar{\boldsymbol{u}}^T)/2$ its scale-filtered version. The second term $\Lambda_{ub}^{\mathrm{MHD}} = \bar{\boldsymbol{b}} \cdot \overline{\mathsf{S}} \cdot \bar{\boldsymbol{b}}$ represents the effect of the large-scale flow to stretch or bend the magnetic field lines, and the final term on the RHS, $2\mu \overline{\mathsf{S}} \colon \overline{\mathsf{S}}$, is the dissipation of (filtered) kinetic energy due to viscous effects. For a detailed description of the terms in Equation (3), see H. Aluie (2017).

### 2.2. Vlasov–Maxwell Formalism

One can also obtain the analog of Equation (3) for the VM system (W. H. Matthaeus et al. 2020; Y. Yang et al. 2022). The evolution of the filtered kinetic energy of each species $\alpha$ at a given scale $\ell$ follows

$$\partial_t E_{f_\alpha}^{\mathrm{VM}} + \nabla \cdot \boldsymbol{J}_{u_\alpha}^{\mathrm{VM}} = -\Pi_\alpha^{\mathrm{VM}} - \Lambda_{ub_\alpha}^{\mathrm{VM}} - \Phi_\alpha^{uT}, \tag{4}$$

where (with no sum over $\alpha$ implied) $E_{f_\alpha}^{VM} = \frac{1}{2}\overline{\rho}_\alpha \widetilde{\boldsymbol{u}}_\alpha^2$ is the filtered bulk flow energy for each species $\alpha$; $\boldsymbol{J}_{u_\alpha}^{\mathrm{VM}} = \widetilde{E}_{f_\alpha}\widetilde{\boldsymbol{u}}_\alpha + \overline{\rho}_\alpha \widetilde{\tau}_\alpha^u \cdot \widetilde{\boldsymbol{u}}_\alpha + \overline{\mathsf{P}}_\alpha \cdot \widetilde{\boldsymbol{u}}_\alpha$ is the spatial transport current, with $\overline{\mathsf{P}}_\alpha$ the pressure tensor, and $\Pi_\alpha^{\mathrm{VM}} = -(\overline{\rho}_\alpha \widetilde{\tau}_\alpha^u \cdot \nabla) \cdot \widetilde{\boldsymbol{u}}_\alpha - \frac{q_\alpha}{c}\overline{n}_\alpha \widetilde{\epsilon}_\alpha^b \cdot \widetilde{\boldsymbol{u}}_\alpha$ is the subscale flux of bulk flow energy across scales due to nonlinearities, with $q$ the charge, $\overline{n}$ the filtered number density, and $c$ the speed of light. Here $\widetilde{\tau}_\alpha^u = \widetilde{\boldsymbol{u}_\alpha \boldsymbol{u}_\alpha} - \widetilde{\boldsymbol{u}}_\alpha \widetilde{\boldsymbol{u}}_\alpha$ is the subscale Reynolds stress and $\widetilde{\epsilon}_\alpha^b = \widetilde{\boldsymbol{u}_\alpha \times \boldsymbol{b}} - \widetilde{\boldsymbol{u}}_\alpha \times \widetilde{\boldsymbol{b}}$ is the subscale electromotive force related to the electric field generated by the subscale magnetic field and subscale velocity. Similarly, $\Lambda_{ub_\alpha}^{\mathrm{VM}} = -q_\alpha \overline{n}_\alpha \widetilde{\boldsymbol{E}} \cdot \widetilde{\boldsymbol{u}}_\alpha$, with $\widetilde{\boldsymbol{E}}$ being the coarse-grained electric field, is the rate of conversion of fluid flow energy into electromagnetic energy through filtered $\boldsymbol{j}_\alpha \cdot \boldsymbol{E}$, and $\Phi_\alpha^{uT} = -(\overline{\mathsf{P}}_\alpha \cdot \nabla) \cdot \widetilde{\boldsymbol{u}}_\alpha$ is the filtered pressure–strain interaction that corresponds to the rate of conversion of flow energy into internal energy for each species $\alpha$.

### 2.3. Comparing Dissipation in the Two Models

Even though these two plasma models are based on different assumptions and approximations, the MHD energy equation should still be comparable to the VM energy equation, provided we consider that the momentum and flow energy are carried mainly by the ion species. (Consideration of electric current density would likewise involve the electron flow properties, but we do not consider these here.) Consequently, we may make an analogy between corresponding terms in Equations (3) and (4); see Figure 1. Clearly, the first term on the left-hand side (LHS) of each equation represents the time rate of change of the flow energy and the second LHS terms represent spatial transport effects. Likewise, the first term on the RHS represents the subscale flux (or the kinetic energy cascade) term. The second RHS term quantifies the conversion of kinetic energy to magnetic energy at scales $>\ell$.

The final terms are also expected to be analogous. This implies that the (collisionless) $\Phi^{uT}$ term has the same effect as the (collisional) viscous dissipation term $2\mu \overline{\mathsf{S}} \colon \overline{\mathsf{S}}$, suggesting that the filtered pressure–strain interaction acts as a viscous dissipation term in VM systems. Recall that most of the

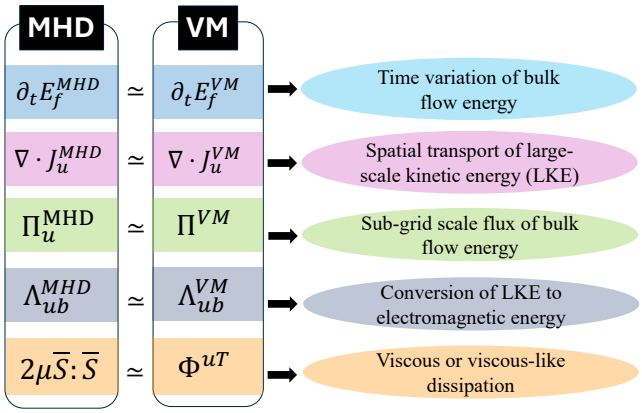


**Figure 1.** Comparing different terms in the scale-filtered kinetic energy density equation obtained using the magnetohydrodynamic (MHD) and Vlasov–Maxwell (VM) formalisms.

momentum is carried by ions and the dissipation term in the ion equation would then most closely correspond to the viscous dissipation in the simple single fluid MHD model.[5] Thus, using this analogy, we propose to write

$$2\mu\overline{\mathsf{S}}:\overline{\mathsf{S}} \sim \Phi^{uT} = -\overline{p}\,\nabla\cdot\widetilde{\boldsymbol{u}} - \overline{\Pi}:\widetilde{\boldsymbol{D}}. \tag{5}$$

For simplicity, we have removed the subscript $\alpha$ from Equation (5), since hereafter we consider only properties of the ions in the VM case. In the usual way, we decompose $\Phi^{uT}$ using $\overline{p}_\alpha = \overline{\mathsf{P}}_{\alpha,ii}/3$, $\overline{\Pi}_{\alpha,ij} = \overline{\mathsf{P}}_{\alpha,ij} - \overline{p}_\alpha\delta_{ij}$, and $\widetilde{D}_{\alpha,ij} = (\partial_i\widetilde{u}_{\alpha,j} + \partial_j\widetilde{u}_{\alpha,i})/2 - (\nabla\cdot\widetilde{\boldsymbol{u}}_\alpha)\delta_{ij}/3$. Here $-\overline{p}\,\nabla\cdot\widetilde{\boldsymbol{u}}$ and $-\overline{\Pi}:\widetilde{\boldsymbol{D}}$ denote the isotropic and anisotropic contributions to the pressure–strain interaction, respectively (see, e.g., Y. Yang et al. 2022).

If one now takes the ensemble average and assumes that the dynamic viscosity $\mu$ is constant and independent of $\overline{\mathsf{S}}$ for a given lag, then $\mu$ at any given scale $\ell$ can be calculated as

$$\mu(\ell) \sim \frac{\langle\Phi^{uT}\rangle}{2\langle\overline{\mathsf{S}}:\overline{\mathsf{S}}\rangle} = \frac{\langle -\overline{p}\,\nabla\cdot\widetilde{\boldsymbol{u}}\rangle - \langle\overline{\Pi}:\widetilde{\boldsymbol{D}}\rangle}{2\langle\overline{\mathsf{S}}:\overline{\mathsf{S}}\rangle}. \tag{6}$$

Finally, the kinematic viscosity can be calculated as $\nu(\ell) = \mu(\ell)/\rho$.

There is a slight complication associated with the above analogy since the VM model is compressible and it is being compared with incompressible MHD. Therefore, we use $\sim$ to relate the first two terms in Equation (6), postulated to be approximately equal in the simulations presented in this study, which are nearly incompressible. If we were to consider strongly compressible VM simulations then in the above equation a suitable approximation could be obtained by eliminating the $\langle -\overline{p}\,\nabla\cdot\widetilde{\boldsymbol{u}}\rangle$ term in the numerator and replacing $\langle\overline{\mathsf{S}}:\overline{\mathsf{S}}\rangle$ by $\langle\overline{\mathsf{D}}:\overline{\mathsf{D}}\rangle$ in the denominator.

We note that a recent study of the Helmholtz decomposition (S. Adhikari et al. 2025) of the pressure–strain interaction has shown that Pi-D ($-\overline{\Pi}:\widetilde{\boldsymbol{D}}$) contains a compressive element within it. By definition, $\boldsymbol{D}$ excludes the contribution of isotropic compression. However, using Helmholtz decomposition if one separates velocity field $\boldsymbol{u}$ into irrotational $\boldsymbol{u}^c$ ($\nabla\times\boldsymbol{u}^c = 0$) and solenoidal $\boldsymbol{u}^s$ ($\nabla\cdot\boldsymbol{u}^s = 0$) components, it is evident that the contribution of $\boldsymbol{u}^c$ is embedded in $\boldsymbol{D}$. Since the VM simulation we employ here is nearly incompressible, this contribution should be negligible.

A similar analogy is expected to hold for the magnetic energy evolution equations in MHD and VM systems, although investigation of this is also deferred to a later study. Note that Equation (3) is not valid for electrons and so one cannot use the analogy to estimate an electron viscosity. Instead, in Section 4.4 we will make use of a different approach, one based on theory, to estimate an effective viscosity for electrons.

In what follows, our approach is to employ scale filtering on data obtained from particle-in-cell (PIC) simulations of decaying turbulence to estimate an effective ion viscosity. We then perform MHD and two-fluid simulations—with the viscosity set to the value estimated from the PIC simulation—and compare the dynamics between these three types of simulations.

The remainder of the paper is organized as follows: in Section 3 we discuss the details of the simulations, with Section 4 presenting estimates for the effective viscosity and analysis of the results. Section 5 provides the conclusions and implications of this study.

## 3. Simulations

We analyze three different types of freely decaying (unforced) simulations. First, we perform fully kinetic PIC simulations of decaying turbulence using the P3D code (A. Zeiler et al. 2002) and use the outputs to estimate the effective viscosity via Equation (6). Second, we perform two-fluid (electron inertial Hall-MHD; EIHMHD; N. Andrés et al. 2014) and MHD simulations with initial conditions set to be very similar to those of the main PIC run, and resistivity and viscosity equal to the (effective) viscosity estimate obtained from the PIC simulation.

All simulations are performed in a 2.5D setup with turbulent fluctuations in the $X$–$Y$ plane but no spatial variation in the $Z$-direction. Results are presented in normalized P3D units where lengths are normalized to the ion inertial length $d_i = c/\omega_{pi}$, with $c$ the speed of light and $\omega_{pi}$ the ion plasma frequency. Time is normalized to the inverse of the proton cyclotron frequency, $1/\omega_{ci}$, and speeds to the Alfvén speed: $V_A = B_0/\sqrt{4\pi n_0 m_i}$ calculated using $B_0$, the arbitrary normalizing magnetic field, and $n_0$ the normalizing density.

For the PIC simulations the domain is a periodic square of side $L_{\rm box} \simeq 150\,d_i$ with 4096 grid points along each Cartesian axis. For each species there are 3200 particles per grid cell (PPG), yielding about 107 billion total particles. The grid spacing is the electron Debye length $dx = \lambda_{D_e}$, the mass ratio is $m_i/m_e = 25$, background density $n = 1n_0$, and the plasma beta for both species is the same: $\beta_i = \beta_e = 0.6$. In these units the wavenumbers $k$ corresponding to the proton inertial ($k_{d_i}$), electron inertial ($k_{d_e}$), and Debye ($k_{\lambda_D}$) scales are located at 23.8, 120, and 628 $k_{\rm box}$, respectively, with $k_{\rm box} = 2\pi/L_{\rm box}$. Initially, the rms fluctuation in velocity and magnetic field are equal: $\delta b_{\rm rms} = \delta v_{\rm rms}$. Initial conditions are created using random phased fluctuations for those Fourier modes whose wavenumbers satisfy $2k_{\rm box} \leqslant k \leqslant 4k_{\rm box}$. The system is evolved without external forcing for more than $10\,\tau_{\rm nl}$, where $\tau_{\rm nl}$ is the nonlinear time estimated as $\tau_{\rm nl} = L_{\rm box}/\delta Z$, with $\delta Z = \sqrt{(\delta v_{\rm rms})^2 + (\delta b_{\rm rms})^2}$ the turbulence amplitude. Such initializations are typical of the Alfvénic initial conditions used in

[5] One should keep in mind, however, that the MHD model is characterized by a single fluid flow velocity, while in the VM system there are separate velocities associated with each particle species. But the disparity of ion and electron masses causes most of the momentum at the scales of current interest to be carried by ions. Very small systems might act differently, as in, for example, electron-only reconnection (T. Phan et al. 2018).

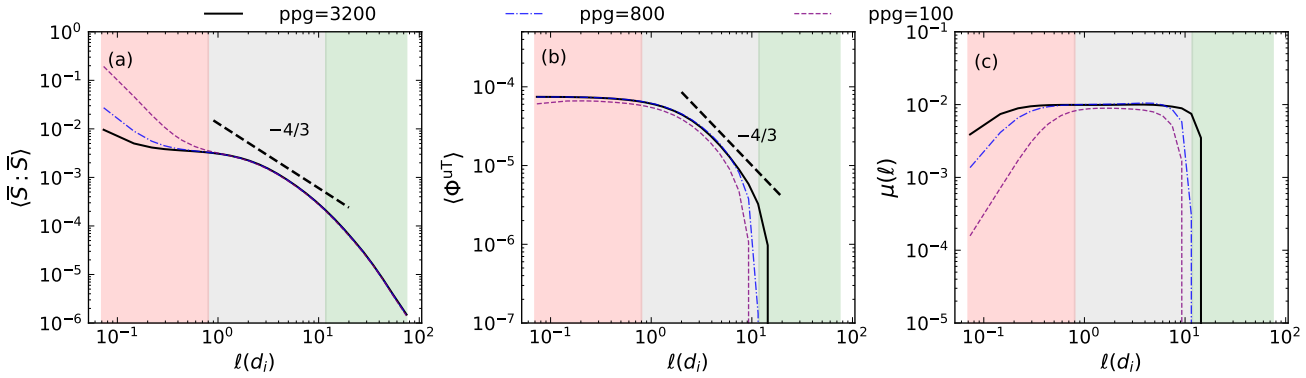


**Figure 2.** Scaling of (a) squared and traced scale-filtered rate-of-strain tensor, (b) filtered pressure–strain interaction, and (c) estimate of ion viscosity, all as obtained from PIC simulations. Results from three simulations with different values for the number of particles per grid cell (PPG) are shown. An $\ell^{-4/3}$ line (black dashed) is drawn for reference.

decaying simulations of MHD turbulence (R. Bandyopadhyay et al. 2018).

In addition to this main PIC simulation we perform several others, where either the PPG count is reduced or the initial ion plasma beta is varied. These provide information regarding scalings and numerical convergence.

For the fluid MHD simulations, both types, the domain is a periodic square box of side $L = 2\pi L_0$, where $L_0$ is a characteristic length. To facilitate comparison of the fluid and VM models we choose $L_0$ to correspond to the correlation scale ($\approx$ the energy-containing scale) of the initial fluctuations, themselves chosen to be equivalent to the initial $\boldsymbol{u}$ and $\boldsymbol{b}$ in the PIC simulation. Thus, $L_0 = \int [E(k)/k]dk / \int E(k)\, dk$, where $E(k)$ is the spectral energy density at wavenumber $k$. The aliasing effects are suppressed by imposing $k_{\max} = N/3$ as the maximum nonzero wavenumber. Here $N = 4096$ is the total number of grid points along each Cartesian direction.

A notable feature of this study is that the MHD simulations are initiated with equal viscosity and resistivity; the values are based on the estimation given in Equation (6) from the PIC simulation. The MHD/fluid runs adopt a value of total plasma $\beta = 1$. For the EIHMHD run, we use the same mass ratio employed in the PIC runs ($m_i/m_e = 25$), so that $k_{d_i} \simeq 25$, and $k_{d_e} \simeq 125$. Run parameters are such that the dissipation wavenumber, $k_{\rm diss}(t) = \langle j^2 + \omega^2 \rangle^{1/4} / \sqrt{\nu}$, where $\nu$ is the kinematic viscosity, has a maximum that is larger than $k_{d_e}$; specifically, $\max_t \{k_{\rm diss}(t)\} \sim 154$. This ensures that the EIHMHD run resolves the electron dynamics.

## 4. Results

### 4.1. Effective Ion Viscosity

In Figure 2, we show the trace of the squared rate-of-strain tensor $\langle \overline{\mathsf{S}} : \overline{\mathsf{S}} \rangle$, the filtered pressure–strain interaction $\langle \Phi^{uT} \rangle$, and the effective viscosity $\mu(\ell)$, each as a function of lag $\ell$. Here the angle brackets indicate spatial averaging rather than ensemble averaging. Data are obtained from PIC simulations at $t\omega_{ci} \approx 3.5\, \tau_{\rm nl}$, when the system is in an approximately statistically steady state.

In Figure 2 we divide the lags into three different regions: the energy-containing, inertial, and kinetic ranges; in the figure these are denoted using green, gray, and red background-shaded rectangles, respectively. It is immediately evident from Figure 2 that both $\langle \overline{\mathsf{S}} : \overline{\mathsf{S}} \rangle$ and $\langle \Phi^{uT} \rangle$ are larger in the kinetic range and eventually fall off in the energy-containing range. Moving toward the smaller kinetic range of scales $< d_i$, we note that $\langle \Phi^{uT} \rangle$ stays constant throughout the kinetic range, while $\langle \overline{\mathsf{S}} : \overline{\mathsf{S}} \rangle$ increases as one approaches smaller scales $\ell \leqslant 0.2\, d_i$. To examine this increase we perform additional simulations with reduced numbers of PPG: 800 and 100 versus 3200. We find that $\langle \overline{\mathsf{S}} : \overline{\mathsf{S}} \rangle$ is sensitive to the number of PPG and is inherently affected by the noise associated with the discrete PPG effect.[6] This is clearly an artifact of PIC simulations. The data suggest that the viscosity $\mu(\ell)$ would become constant at very small $\ell$ in the limit of infinite PPG. We note that it may be possible to further analyze this "PIC effect" by explicit evaluation of a graininess factor based on the number of PPG (M. Feix & P. Bertrand 2005). However we will not pursue this here since the sequence of results in Figure 2 already reveals the relevant trend.

The effective viscosity $\mu(\ell)$, Figure 2(c), is found to be constant in the inertial range and part of the kinetic range. The constancy of the effective viscosity in the inertial range can be understood in terms of power scaling. The squared and traced rate-of-strain tensor scales as $(\delta u/l)^2$. Following Kolmogorov-like turbulent energy spectrum, the velocity fluctuations $\delta u$ scale as $\ell^{1/3}$ resulting in $\overline{\mathsf{S}} : \overline{\mathsf{S}} \sim \ell^{-4/3}$. However, the scaling of the pressure–strain interaction is not straightforward to determine from its composition. Since the pressure–strain interaction is the contraction of the pressure tensor with the rate-of-strain tensor, the Fourier transform of the pressure–strain interaction is the convolution of the Fourier transforms of the pressure tensor and the rate-of-strain tensor. As a result, the theoretical scaling of the pressure–strain interaction is difficult to estimate. Empirically, the PIC simulation results seen in Figure 2(b) suggest that the pressure–strain interaction exhibits a $\ell^{-4/3}$ dependence. As a result, the effective viscosity, which is the ratio of the square of the filtered rate-of-strain tensor and filtered pressure–strain interaction, is independent of lag at inertial range scales and also into the kinetic range, displaying an extended plateau at $\mu(\ell) = 0.01$. We denote this plateau value as $\mu^{\rm eff}$ and use it as the estimated value of effective viscosity for ions. At smaller lags, $\mu(\ell)$ falls off, probably due to the particle noise effect, since $\langle \overline{\mathsf{S}} : \overline{\mathsf{S}} \rangle$ increases at these scales. In addition, the maximum lag for the constancy of the effective viscosity also decreases with

[6] Recall that the Vlasov equation formally emerged in the limit of an infinite number of particles per Debye sphere.

reduced PPG. Once again we emphasize that in the limit of an infinitely large number of particles per cell, we expect the effective viscosity to remain constant over a wide range of lag scales and extend all the way to the smallest lag in the system.

In the energy-containing range, the magnitudes of both $\langle \overline{\mathsf{S}}\colon \overline{\mathsf{S}} \rangle$ and $\langle \Phi^{\mu T} \rangle$ are significantly reduced. Moreover, since $\langle \overline{\mathsf{S}}\colon \overline{\mathsf{S}} \rangle$ is positive definite, but $\langle \Phi^{\mu T} \rangle$ is not, using Equation (6) to determine the effective viscosity means it could be negative for some scales, with this being more likely in the energy-containing range. However, since the net viscous dissipation in the energy-containing range is expected to be negligible, there is little need to employ an effective viscosity in this range.

Using the effective viscosity and mean square vorticity $\langle \omega^2 \rangle$, one may calculate the rate of effective viscous[7] dissipation as $D_\mu = \mu^{\rm eff} \langle \omega^2 \rangle$ and compare it with the rate of change of ion-flow energy $-\partial \langle E_f \rangle / \partial t$. At the time of analysis, we find $D_\mu = 1.02 \times 10^{-4}$ and $-\partial \langle E_f \rangle / \partial t = 9.19 \times 10^{-5}$. The approximate equivalence of these values provides a validation of the effective viscosity approach.

The effective viscosity estimated above is the dynamic viscosity of ions. We may also calculate an effective kinematic viscosity, $\nu^{\rm eff} = \mu^{\rm eff}/\langle \rho \rangle = 0.01$, where $\langle \rho \rangle = m_i \langle n_i \rangle = 1$ is the mass density since both the mass and the ion density are unity in the setup for this run.

We may compare these results to those obtained via an alternative (non-scale-filtering) approach for estimating an effective viscosity (Y. Yang et al. 2024b). In that approach, the effective viscosity is not determined as a function of scale so that the estimate would probably account for the viscosity at the smallest scale in the simulation. Adopting this correspondence, the effective viscosity estimate $\mu^{\rm eff}_{\ell \sim 0.06} = 3.9 \times 10^{-3}$ (see Figure 2(c)) is close to the estimate obtained by Y. Yang et al. (2024b), $\mu = 5.31 \times 10^{-3}$.

### 4.2. Kolmogorov Scales and Reynolds Number

Having accomplished an estimation of effective viscosity for nearly collisionless plasma turbulence, we can now calculate the (effective) Kolmogorov scales for length $\eta$, time $\tau_\eta$, and velocity $u_\eta$ (A. N. Kolmogorov 1941; U. Frisch 1995). For an incompressible fluid these scales, by definition, depend only on the (spatially averaged) total energy dissipation rate (per mass) $\epsilon$ and the kinematic viscosity $\nu$:

$$\eta = \left(\frac{\nu^3}{\epsilon}\right)^{1/4}, \quad \tau_\eta = \left(\frac{\nu}{\epsilon}\right)^{1/2}, \quad u_\eta = (\nu\epsilon)^{1/4}. \tag{7}$$

For the kinetic system, the energy dissipation rate can be calculated using the time rate of change of the volume-averaged magnetic $\langle E_B \rangle$ and ion-flow $\langle E_{if} \rangle$ energies,[8] i.e.,

$$\langle \rho \rangle \epsilon = -\partial \langle E_B + E_{if} \rangle / \partial t \doteq 5.31 \times 10^{-4}. \tag{8}$$

Here we have employed the approximation, akin to Favre averaging, that $\langle \rho(\boldsymbol{x}) \epsilon(\boldsymbol{x}) \rangle \approx \langle \rho \rangle \epsilon$ on the LHS. Employing this estimate for $\epsilon$ in Equation (7), and setting $\nu = \nu^{\rm eff}$, yields $\eta = 0.20$, $\tau_\eta = 4.34$, and $u_\eta = 0.048$. The Reynolds number based on the large-scale flow features can be computed using

$$Re = \left(\frac{L}{\eta}\right)^{4/3} = 135, \tag{9}$$

where $L$ is the correlation length estimated using an average value of the initially excited Fourier wavenumbers, viz. $L = 1/k_{\rm av} = L_{\rm box}/(3 \times 2\pi) = 7.93$. This is consistent with the approximately 1 decade inertial range present in this system (see T. N. Parashar et al. 2018; S. Adhikari et al. 2021). We remark that this estimated Reynolds number is smaller than the estimate provided in Y. Yang et al. (2024b), primarily because the effective viscosity estimated in this paper is approximately twice the estimate of Y. Yang et al. (2024b).

### 4.3. Ion Viscosity and Temperature

Next we explore the effect of plasma beta $\beta$ on the effective viscosity of ions, by analyzing three additional runs with the same initial conditions but different ion $\beta$ values, namely 0.03, 0.3, and 1.2. The value of $\beta$ is adjusted by changing the (initial) ion temperature. As is seen in Figure 3, we find that the (plateau) effective viscosity, $\nu^{\rm eff}$, increases with increasing ion plasma $\beta$ (and thus, with increasing ion temperature). While previous studies have shown an inverse dependence of viscosity on temperature in dusty plasmas (Z. Haralson & J. Goree 2016), the present finding is consistent with the effect of temperature on the viscosity of neutral gases.

### 4.4. Effective Electron Viscosity

Although it is invalid to use Equation (6) directly for electrons, we may still estimate an effective electron viscosity by exploiting a relationship between it and the ion viscosity. Following S. Braginskii (1965), there has been some significant progress in estimating the collisional viscosities for ions and electrons in fully ionized plasmas for all values of the ion charge $Z$ (K. Whitney 1999). For a collisional electron–proton plasma the ratio of ion and electron viscosities behaves as (A. Velikovich et al. 2001)

$$\frac{\mu_i}{\mu_e} = \left(\frac{T_i}{T_e}\right)^{5/2} \left(\frac{m_i}{m_e}\right)^{1/2}. \tag{10}$$

As an exercise, we may apply the above result to our (essentially collisionless) PIC simulations $m_i/m_e = 25$ and $T_i/T_e = 1$, so that $\mu_e = \mu_i/5 = 2 \times 10^{-3}$. For magnetospheric multiscale mission (MMS) observations typical temperature ratios are $T_i/T_e = 5$ (C.-P. Wang et al. 2012), and using the true physical mass ratio $m_i/m_e = 1836$, Equation (10) yields $\mu_i \simeq 2400\, \mu_e$, suggesting that the ion viscosity could be much larger than the electron viscosity.

On the other hand Y. Yang et al. (2024b) using MMS data found a different result, namely that $\mu_i/\mu_e \simeq 150$. This difference may be due to inaccuracy of the approximation in Equation (10) for plasmas of low collisionality such as the magnetosheath. We note also that Y. Yang et al. (2024b) used a relation similar to Equation (6) for electrons as well as ions.

### 4.5. Comparison with Two-fluid and MHD Simulation

In this subsection, we compare the energetics of our main kinetic (PIC) simulation with results from the two-fluid (EIHMHD) and MHD simulations. Recall that these are

[7] Here we are neglecting compressive contributions to viscous dissipation, which, in a fluid model, would be $\propto \zeta \langle (\nabla \cdot \boldsymbol{u})^2 \rangle$, where $\zeta$ is the bulk viscosity.

[8] The rate of change of electron flow energy is negligible relative to the net dissipation in the system (Y. Yang et al. 2024a).

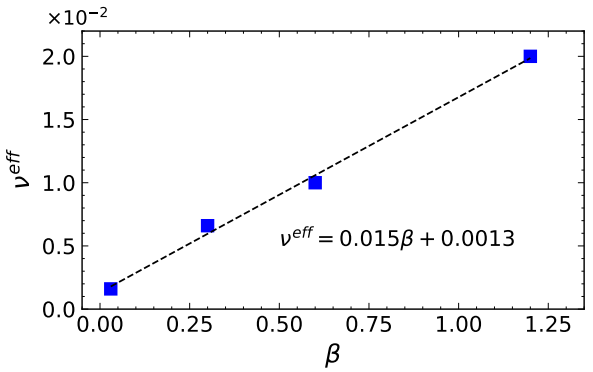


**Figure 3.** Effective viscosity of ions as a function of ion plasma beta. The dashed line is the line of best fit.

performed with initial conditions very similar to those of the PIC run and using a viscosity equal to the (inertial range plateau) effective viscosity estimate obtained from the PIC simulation. Note, however, that because the PIC and fluid codes employ different normalizations and domain sizes, $\nu^{\rm eff}_{\rm PIC} = 0.01\, V_A d_i$ corresponds to $\nu^{\rm eff}_{\rm fluid} = 0.01 \times (2\pi/L_{\rm box})\, V_A L_0$ for both the fluid cases, where $L_{\rm box}$ is the length of the box for the PIC simulation.

In Figure 4(a) we compare the time evolution of the magnetic energy and ion-flow energies for these three cases. The change in magnetic energy in the two-fluid case overlaps almost perfectly with the PIC results, while the magnetic energy in MHD has a slightly (∼10%) larger value during the period 2–4 $\tau_{\rm nl}$. Turning to the (change in) the ion-flow energy for these runs, these also follow each other very closely until about 2 $\tau_{\rm nl}$. At later times, the two-fluid and MHD simulations both show smaller decreases (≈10%) in ion-flow energy compared to the kinetic case. The slight discrepancy toward the end is possibly due to the differences in channels of energy transfer and dissipative mechanisms in these systems. For example, the pressure–strain interaction, a pathway that relates flow energy to thermal energy, is absent in both the MHD and EIHMHD cases.

Figure 4(b) displays the time evolution of the rms value of the (normalized) out-of-plane electric current density, $j_z$, across these three simulations. Here too, the evolutions are rather similar, particularly in the period where $j_{z,\rm rms}$ is approximately steady ($\tau_{\rm nl} \sim 3$–4), corresponding to well-developed turbulence. During the early and late phases of the simulations, $j_{z,\rm rms}$ levels for both of the fluid runs fall below the level from the kinetic simulation. This is because in the PIC case, the initial magnetic islands and subsequent secondary islands can interact at the electron scales, resulting in a sharp gradient of the magnetic fields and therefore larger out-of-plane currents.

In Figure 5, we compare the magnetic and kinetic energy spectra for these three cases at the time of analysis $t = 3.5\tau_{nl}$. Clearly, the magnetic energy spectra are almost identical at the intermediate wavenumbers $3 \leqslant k \leqslant 50$, following a $-5/3$ Kolmogorov-like spectrum. This suggests that these systems, initialized with identical conditions, follow similar time evolution in the inertial range. While the magnetic spectra for PIC follow MHD closely at higher wavenumbers, the spectra for EIHMHD deviate from the MHD and PIC and exhibit a relatively steeper slope. At large wavenumbers, we see a small peak for the magnetic energy spectrum for PIC, which is often characterized to the discrete particle effect (noise). The inset of Figure 5 shows that the kinetic energy

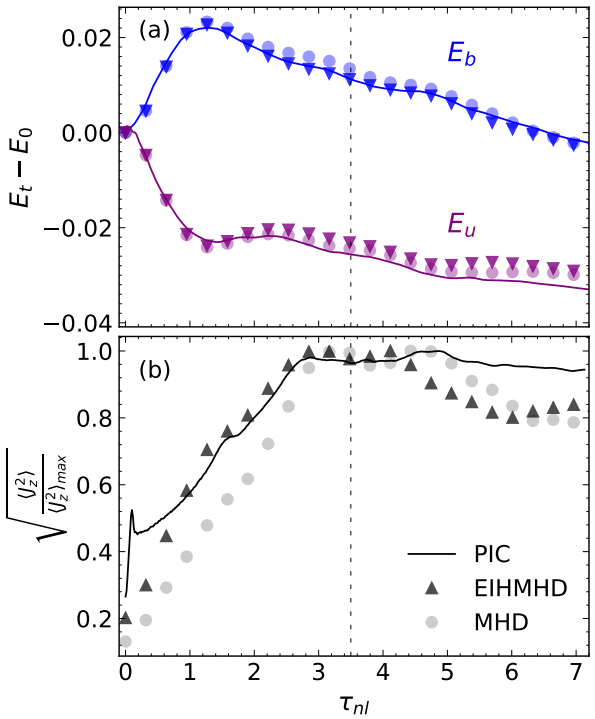


**Figure 4.** Time evolution of some equivalent quantities from the kinetic, two-fluid, and MHD simulations: (a) the change in spatially averaged magnetic energy $E_b$ and ion-flow energy $E_u$, and (b) the normalized rms out-of-plane electric current density, $j_z$. Normalization of the rms $j_z$ is with respect to its maximum in the time series. Note that the viscosity in the two-fluid and MHD simulations is equivalent to the effective viscosity obtained from the PIC simulation. The vertical dashed line denotes the time of analysis used in connection with Figure 2.

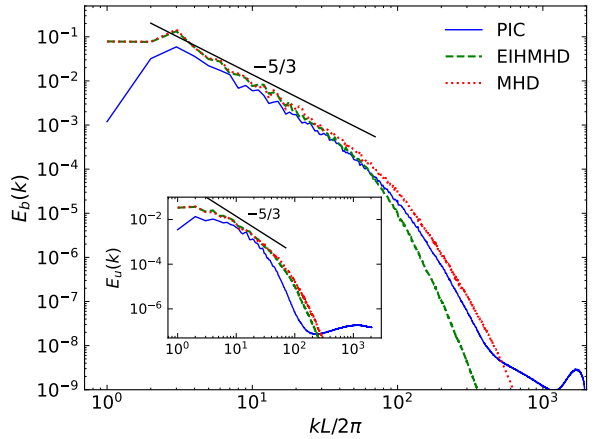


**Figure 5.** A comparison of the magnetic energy spectra for MHD, EIHMHD, and PIC simulations at the time of analysis $t = 3.5\tau_{nl}$, shown by the dashed line in Figure 4. In the inset we compare the kinetic energy spectra. The solid reference lines correspond to a slope of $-5/3$.

spectra of these three cases follow each other closely for wavenumbers $3 \leqslant k \leqslant 50$ and exhibit a $-5/3$ slope. However, for $k > 30$, the kinetic energy spectrum for the kinetic case falls off earlier than the other two cases. While the inertial scale features of both the kinetic and magnetic spectra are similar in these systems, there exist some differences in the smaller (large length scale) and larger (smaller length scale) wavenumbers. This is mostly likely due to the differences in energy transfer mechanisms at these scales.

## 5. Conclusion and Discussion

In this paper, using kinetic PIC simulations of nearly collisionless plasma turbulence, we estimate the effective viscosity. We use a scale-filtering (or coarse-graining) approach to compare the time evolution equation of the flow energy in both MHD and VM formalisms. We find that the effective viscosity, while formally scale dependent, becomes independent of scale in the inertial range and even into the kinetic range. We hypothesize that the decrease in the value of the effective viscosity seen at the smallest scales is solely due to the limited number of PPG used in our PIC simulations. Therefore our conjecture is that for arbitrarily large numbers of particles per cell, the derived effective viscosity would become constant down to arbitrarily small lags. At the larger (e.g., energy-containing range) scales, effective viscosity is insignificant, since the net dissipation at those scales is negligible.

There are also interesting differences in runs with different PPG in the large-scale end of the inertial range and into the energy-containing range. While almost no difference with variation in PPG is seen in the scale-filtered trace of the rate of strain at these outer scales, there are quite noticeable deviations in the PPG dependence of the pressure–strain and the effective viscosity as scales approach the correlation length. But the effective viscosity becomes negligible at these scales, so the disparity with varying PPG becomes of less importance.

We also performed an MHD and a two-fluid simulation with initial conditions that are almost identical to those of the PIC run. For these runs the imposed values of viscosity and resistivity were set equal to the effective viscosity obtained from the PIC simulation. Upon comparing the results of these three cases, we found striking similarities in the global behavior of magnetic and ion bulk flow energy. We also found closely similar behaviors in the time history of the out-of-plane current densities, particularly near the time of maximum dissipation. These consistent aspects of the three types of simulations provide validation of the main result, which is the method for estimation of the effective viscosity.

It is relevant to note that a complementary alternative approach to quantifying collisionless dissipation may be based on analysis of the velocity space, and in particular phase mixing (H. Wiechen 1999). The literature on this approach (D. Grasso et al. 2001; A. Ghizzo & D. Del Sarto 2021; A. Ghizzo et al. 2023) exploits the coarse-graining effect of phase mixing in order to estimate the effective collisionless dissipation.

In future work we expect to examine the assumption made in Equation (6) that $\mu$ and $\overline{\mathsf{S}}$ are statistically independent. This should be checked a posteriori using simulation data, even though the constancy of $\mu$ in the results suggests that the approximation is valid.

In computing characteristic turbulence scales based on the effective viscosity we found that the Kolmogorov scale $\eta$ is smaller than the ion inertial length $d_i$. This may seem to be an anomalous result given that $d_i$ is often associated with the spectral break at the termination of the inertial range in the solar wind at order 1 or high plasma $\beta$ (R. J. Leamon et al. 1998; C. Chen et al. 2014). The fact that here the estimated $\eta$ is smaller than $d_i$ seems decidedly not hydrodynamic-like. There is, however, precedent for this, an example being the study of Taylor scale $\lambda_T$ in the solar wind (W. Matthaeus et al. 2008). Normally in hydrodynamics turbulence one expects that $\lambda_T > \eta$. But W. Matthaeus et al. (2008) found that solar winds with low plasma $\beta$ are characterized by estimated values of $\lambda_T < d_i$. This kind of nonhydrodynamic scaling of turbulence parameters is perhaps expected in collisionless plasmas for which there are numerous additional physical length scales present, including those associated with both electrons and ions.

In closing, the present approach for estimating viscosity may have broad application in collisionless plasmas. One immediate extension is to use this technique in analysis of MMS observations. The MMS data sets provide high-resolution measurements that resolve scales as small as electron length scales. This introduces the possibility of computing directly the electron viscosity, which in turn provides a contribution to resistivity.

## Acknowledgments

This research is partially supported by the MMS Theory, Modeling and Data Analysis team under NASA grant 80NSSC19K0565, by the NASA LWS program under grants 80NSSC20K0198 and 80NSSC22K1020 and a subcontract from the New Mexico consortium 655-001, a NASA Heliophysics MMS-GI grant through a Princeton subcontract SUB0000517, and by the National Science Foundation Solar Terrestrial Program grant AGS-2108834. Y.Y. is supported by 2024 Ralph E. Powe Junior Faculty Enhancement Award and the University of Delaware General University Research Program grant. F.P. is supported by NSF SHINE 2501387 at the University of Delaware and a Plan for NASA EPSCoR Research Infrastructure Development (RID) in Delaware (NASA award 80NSSC22M0039). R.B. acknowledges MMS early career award 80NSSC21K1458. This research was also supported by the International Space Science Institute (ISSI) in Bern, through ISSI International Team projects #556 (Cross-scale energy transfer in space plasmas) and #23-588 (Unveiling energy conversion and dissipation in nonequilibrium space plasmas). We would like to acknowledge high-performance computing support from Cheyenne (DOI:10.5065/D6RX99HX) and Derecho (DOI:10.5065/qx9a-pg09) provided by NCAR's Computational and Information Systems Laboratory, sponsored by the National Science Foundation.

## ORCID iDs

Subash Adhikari https://orcid.org/0000-0003-2160-7066
Carlos A. González https://orcid.org/0000-0001-7063-2511
Yan Yang (杨艳) https://orcid.org/0000-0003-2965-7906
Sean Oughton https://orcid.org/0000-0002-2814-7288
Francesco Pecora https://orcid.org/0000-0003-4168-590X
Riddhi Bandyopadhyay https://orcid.org/0000-0002-6962-0959
William H. Matthaeus https://orcid.org/0000-0001-7224-6024

## References

Adhikari, S., Parashar, T. N., Shay, M. A., et al. 2021, PhRvE, 104, 065206
Adhikari, S., Yang, Y., & Matthaeus, W. H. 2025, arXiv:2503.11825
Adhikari, S., Yang, Y., Matthaeus, W. H., et al. 2024, PhPl, 31, 020701
Aluie, H. 2013, PhyD, 247, 54
Aluie, H. 2017, NJPh, 19, 025008
Andrés, N., Gonzalez, C., Martin, L., Dmitruk, P., & Gómez, D. 2014, PhPl, 21, 122305
Bandyopadhyay, R., Wan, M., & Chhiber, R. 2018, PhRvX, 8, 041052
Bandyopadhyay, R., Yang, Y., Matthaeus, W. H., et al. 2023, PhPl, 30, 080702
Braginskii, S. 1965, in Reviews of Plasma Physics, ed. M. Leontovich (New York: Consultants Bureau)

Chen, C., Leung, L., Boldyrev, S., Maruca, B., & Bale, S. 2014, GeoRL, 41, 8081
Coroniti, F. 1980, JGRA, 85, 6719
Favre, A. 1969, Problems of Hydrodynamics and Continuum Mechanics (Philadelphia, PA: SIAM), 231
Feix, M., & Bertrand, P. 2005, TTSP, 34, 7
Frisch, U. 1995, Turbulence. The Legacy of A.N. Kolmogorov (Cambridge, UK: Cambridge Univ. Press)
Germano, M. 1992, JFM, 238, 325
Ghizzo, A., & Del Sarto, D. 2021, PPCF, 63, 055007
Ghizzo, A., Del Sarto, D., & Betar, H. 2023, PhRvL, 131, 035101
Grasso, D., Califano, F., Pegoraro, F., & Porcelli, F. 2001, PhRvL, 86, 5051
Haralson, Z., & Goree, J. 2016, PhPl, 23, 093703
Kolmogorov, A. N. 1941, DoSSR, 30, 301
Leamon, R. J., Smith, C. W., Ness, N. F., Matthaeus, W. H., & Wong, H. K. 1998, JGRA, 103, 4775
Matthaeus, W., Weygand, J., Chuychai, P., et al. 2008, ApJL, 678, L141
Matthaeus, W. H., Yang, Y., Wan, M., et al. 2020, ApJ, 891, 101
Parashar, T. N., Matthaeus, W. H., & Shay, M. A. 2018, ApJL, 864, L21
Pezzi, O., Liang, H., Juno, J., et al. 2021, MNRAS, 505, 4857
Phan, T., Eastwood, J. P., Shay, M., et al. 2018, Natur, 557, 202
Velikovich, A., Whitney, K., & Thornhill, J. 2001, PhPl, 8, 4524
Wang, C.-P., Gkioulidou, M., Lyons, L. R., & Angelopoulos, V. 2012, JGRA, 117, A8
Whitney, K. 1999, PhPl, 6, 816
Wiechen, H. 1999, AnGeo, 17, 595
Yang, Y., Adhikari, S., & Matthaeus, W. H. 2024a, JGRA, 129, e2024JA033105
Yang, Y., Matthaeus, W. H., Roy, S., et al. 2022, ApJ, 929, 142
Yang, Y., Matthaeus, W. H., Oughton, S., et al. 2024b, MNRAS, 528, 6119
Yang, Y., Matthaeus, W. H., Parashar, T. N., et al. 2017, PhPl, 24, 072306
Yang, Y., Wan, M., Matthaeus, W. H., et al. 2019, MNRAS, 482, 4933
Zeiler, A., Biskamp, D., Drake, J., et al. 2002, JGRA, 107, 1230
Zenitani, S., Hesse, M., Klimas, A., & Kuznetsova, M. 2011, PhRvL, 106, 195003